Locating flood embankments using SAR time series: A proof of concept

M. Wood*, S.M. de Jong, M.W. Straatsma

Department of Physical Geography, Faculty of Geoscience, Utrecht University, Princetonlaan 8, 3584 CB, Utrecht, The Netherlands

ABSTRACT

River embankments limit flood risk, alter the flood peak, and change sediment deposition rates, but in many areas of the world embankment locations are not available in geodatabases. This lack of information reduces the accuracy of predicted flood extent within inundation models. The objective is therefore to determine the positional accuracy of embankments using time series of Sentinel-1 Synthetic Aperture Radar (SAR) data with local gauge data. A new method is proposed to: (1) establish the relationship between stage and extent for river cross sections; with stage obtained from gauges and flood extent from SAR-derived flood images, and (2) infer embankment location from plateaus in these plots. The predicted embankment location was compared with airborne LiDAR data for two case studies: the One Hundred Foot Wash (UK) and the Yolo Bypass (Sacramento, USA). The median absolute error for cross sections located in low lying floodplains with low vegetation was 59 m and 110 m, respectively. This increased to 78 m and 197 m when vegetated and cross sections with high ground were included. Application of the method could provide key flood defence information to update geodatabases for locations where data are missing or not widely/freely available, and to improve inundation models up to global scales.

1. Introduction

Floods are responsible for catastrophic loss of life and devastation to livelihoods and communities in poorer parts of the world (Di Baldassarre et al., 2010). Flooding and storms together accounted for 47% of all weather-related disasters from 1995 to 2015, affecting 2.3 billion people, the vast majority living in Asia and in lower-income countries (Wahlstrom and Guha-Sapir, 2015). Projected climate and population changes mean that there is a pressing need to better understand the current and future risk that flood-prone river systems will place on populations and resources around the globe (Alfieri et al., 2017). Real-time flood forecasting and prediction models are being used to meet this need. Strategic flood risk models and model cascades are used to indicate flood impacts and hazards at a range of scales (Pappenberger et al., 2012; Ward et al., 2013; Winsemius et al., 2013; Wu et al., 2014). Global scale inundation models (e.g. CaMa-Flood; Yamazaki et al., 2011) benefit particularly from advances in modelling, computational power and data availability. However, inherent model uncertainties are often not clearly quantified for end users (Trigg et al., 2016). And one key area of uncertainty in inundation models is topography data. Topography data serves as model input to inform flow direction, the location and size of river channels and off-line storage, as well as the smaller connectivity pathways. As a result, Airborne Light Detection and Ranging (LiDAR) and Earth observing satellites are becoming increasingly important resources for accurate topography in large scale models (Bates 2012). For global models, Digital Elevation Models (DEMs) from satellites present an attractive alternative to airborne LiDAR DEMs, which suffer from being neither globally nor freely available (Schumann et al., 2014). Satellite derived DEMs that are relevant for flood modelling range between 12 m and 90 m in spatial resolution and between 2 m and 17 m in vertical accuracy (Table 1). However, line elements such as embankments are not always adequately represented in Satellite derived DEM products. Even with advances in flood modelling capability and global DEM accuracy, key structural flood defence information may still be missing, or be drawn from broad assumptions. In many areas of the world the location and height of structures such as flood embankments are not recorded adequately or at all, and large efforts have to be made to collect these data (Nicholas and Mitchell, 2003). This is especially true for data-poor locations, such as Bangladesh and Mozambique.

The presence of hard defences not only reduces flood risk, but also affects the hydro-economic system by altering flood wave celerity, peak levels and sediment deposition rates. If large scale flood models cannot provide accurate and up-to-date information on flood protection and defence standards due to missing data, then services such as global-scale flood mapping (Pappenberger et al., 2012; Schellekens et al., 2014) and web-based hazard mapping services (e.g. GloFAS: Alfieri et al., 2013 and GFMS: Hong et al., 2007; Scussolini et al., 2016; Wu

---

Table 1
Overview of global scale Digital Elevation Model products.

Product	Spatial Resolution (m)	Relative Vertical Accuracy (m)	Reference
TanDEM-X	12	2	Krieger et al. (2007)
MERIT DEM	90	2	Yamazaki et al. (2017)
ALOS World 3D	30	5	Tadono et al. (2014); Takaku et al. (2014)
Shuttle Radar Topography Mission (SRTM)	30	10	Farr et al. (2007)
ASTER GDEM2	70	17	Tachikawa et al. (2011)

et al., 2014) would be undermined also.

The solution could be to map the location of flood defence features with help of satellite imagery. However, the scientific literature on detecting flood defence structures remotely for data-poor locations is sparse. While the advantages of using visible and infra-red data (e.g. MODIS, Landsat series) satellites to characterise environmental changes have been known for decades (e.g. Deutsch and Estes, 1980; Imhoff et al., 1987; Hu et al., 2009; Woodcock et al., 2001), these data can be limited by issues of temporal availability, cost or weather conditions. However, studies which locate surface features with other, more weather-penetrating, frequencies are scarce. Only one study could be found which mapped location of surface features with radar imagery (Blom et al., 1984). Instead research has concentrated on finding un-documented structures with LiDAR (Briese, 2004; Czuba et al., 2015; Krüger and Meinel, 2008) or using DEM data with active contour methods to outline dike locations (Gang et al., 2003). Additionally, the use of photogrammetry and SAR products from Uninhabited Aerial Vehicle SAR (UAVSAR) is becoming more widespread to support local (high-resolution/low-cost) embankment structural health monitoring (Carvajal et al., 2011; Dabbiru et al., 2014; Marapareddy et al., 2016) or to enhance multi-spectral satellite observations (Gruen et al., 2012). The studies which do utilise radar satellite data, particularly the data from the second generation of SAR satellites, focus on the structural changes of buildings, dams, wetlands, railway infrastructure and cultural heritage areas (Chang et al., 2014; Milillo et al., 2016; Nico et al., 2015; Schmitt and Brisco 2013; Schmitt et al., 2014; Tomás et al., 2013; White et al., 2015).

SAR satellite instruments can capture images of the Earth day or night, and independent of weather conditions (ESA/SAR, 2017). Flood mapping using SAR data has been a long-term research topic, evolving from simple mapping of flood extent (Biggin and Blyth 1996; Imhoff et al., 1987; Niedermeier et al., 2000; Oberstadler et al., 1997; Pulvirenti et al., 2011), to deriving water elevations by intersection of flood edge with a DEM (Mason and Davenport, 1996), flood edge refinement algorithms (Horritt et al., 2001; Mason et al., 2007) and assimilation of SAR data to improve flood models (Horritt, 2006; Hostache et al., 2009; Lai and Monnier 2009; Montanari et al., 2009; Wood et al., 2016). Further post-processing of SAR imagery using techniques such as histogram thresholding (Martinis et al., 2009; Matgen et al., 2007, 2011), texture analysis (Herold et al., 2004; Pradhan et al., 2014) and fuzzy logic (Pulvirenti et al., 2011) to classify water enabled the creation of water maps. Although issues of speckle, noise and misclassification errors (e.g. from wind roughening of surfaces, scatter or bounce effects) can all detrimentally affect accuracy of these maps. Consequently additional post-processing techniques like region growing and change detection have been employed to improve classification (Giustarini et al., 2013; Lu et al., 2014; Mason et al., 2010; Schlaffer et al., 2015).

Despite the clear advantages of using SAR satellites to map the spatio-temporal movement of water, the presence of vegetation has been shown to frustrate detection of the water edge by scattering the return signal (Horritt et al., 2001; Mason et al., 2010). Early studies of edge detection used an active contour model and ERS-1 SAR imagery to identify 75% of the flooded area correctly, with 70% of the waterline coinciding with ground data within 20 m (Mason and Davenport, 1996). ERS SAR products have 26 m×30 m spatial resolution

(EOPORTAL, 2017). More recent studies with synthetic and ERS SAR satellite products using fuzzy connectivity, wavelet and active contour methods (Dellepiane et al., 2004; Horritt et al., 2003; Horritt, 1999; Niedermeier et al., 2000) were validated using finer resolution aerial photography and LiDAR data. These studies reported mean errors of between 2.5 and 3.5 pixels with the ERS data (approximately 65 m–105 m) and 120 m for the synthetic SAR data (reduced to just 70 m when corrected for vegetation effects). These studies mapped shoreline locations with SAR data. No studies could be found that mapped inland flood structure or embankment location with SAR data.

There is a demand for flood defences information to improve flood models for inaccessible and data-sparse locations, or over large areas. Therefore, the aim of this paper is to locate flood embankments using time series of SAR data combined with water levels measured at gauging stations. The rationale of the method is that flood extent remain identical over a range of water levels once the flood extent has reached the toe of the embankment. Specifically, the objectives are: (i) to develop a method to determine the location of river embankments using a time series of SAR satellite data combined with local gauge data; (ii) to determine the positional accuracy of the methodology against reference data, and (iii) asses the sources of error. An ancillary objective is to examine the sensitivity of the resulting embankment position to the settings in the method of processing the SAR imagery. To prove the concept we applied it to two test locations; one at the One Hundred Foot Wash, Cambridgeshire, UK and the other at the Sacramento River Bypass system at Yolo, California, USA.

2. Method

Flood expansion and contraction can be mapped using multi-temporal satellite observations (Mason et al., 2007; Pulvirenti et al., 2011) and it is observations of the moving boundary of this flood edge that is examined here. For this study flood extent refers to the distance between the river centre to the (left or right side) flood edge, along a given cross section. All cross sections are orientated perpendicular to the river's axis. The flood extent for both left and right of river centre are measured separately (green and orange horizontal line colours respectively, in Fig. 1). The concept is that a sequence of observations of flood extent can indicate the location of high flood defences. The method presented here consists of establishing stage-extent relationships for a given (left or right side) cross section. The relationship is illustrated in Fig. 1a which shows a single cross section of a river and floodplain, in side view, with a range of potential flood extents, between the river centre and adjacent embankments, as flood levels (stage) rise and fall.

Fig. 1b shows a plot of the evolution of the flood level-extent relationship shown in Fig. 1a. This is the key feature of the proposed methodology. In Fig. 1b, flood extent is plotted on the y-axis and gauged water level (i.e. stage) is plotted on the x-axis. If lateral flood extent increases, but water levels do not, floodwaters are expanding within the floodplain and this is represented by a strong vertical line in Fig. 1b. Conversely, if flood extent stops expanding, but water levels yet increase, this is evidence of an obstruction to flood expansion, and is represented by a strong horizontal line in Fig. 1b. When the flood extent resumes expanding vertically after a horizontal plateau it is asserted that a structure has been overtopped at that point. The proposed methodology exploits this stage-extent relationship, and critically
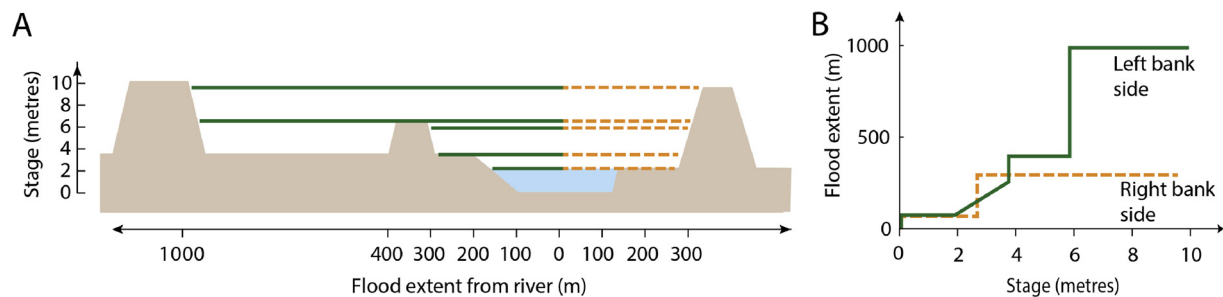
Fig. 1. A) river cross-section, illustrating the relationship between water level (stage) and flood extent. B) Conceptual 'stage-extent' plot showing the expected relationship between water level (x-axis) and one-sided flood extent (y-axis) to infer location of flood defence structures. Orange lines indicate the right bank side of the river and green lines indicate the left bank side of the river. (For interpretation of the references to colour in this figure legend, the reader is referred to the web version of this article.)

searches for extended horizontal lines at each cross section, to infer the position of flood embankments.

The following method section therefore has two parts: Part 1 concerns the processing of SAR imagery into fluvial flood maps, which are the areas that are inundated by river water. Part 2 describes the implementation of the stage-extent plot and the derived embankment location for designated cross sections. An explanation of the validation and sensitivity testing methodology is provided in Sections 2.3 and 2.4, followed by data and test locations used (Section 3).

2.1. Part 1: deriving fluvial flood maps from SAR imagery

The large textural contrast in SAR images between smooth water surfaces and rougher land areas makes time series of SAR data a useful tool in mapping flood extent. Sentinel-1 SAR data were used because of its large spatial coverage, short revisit times and its wide availability. The details of the Sentinel-1 data products used are provided in section 3.3.

2.1.1. Creating binary water maps from SAR data

Pre-processed and geo-referenced Level 1 Sentinel-1 data were downloaded, then each SAR product was calibrated, terrain-corrected and clipped using ESA's SNAP software (ESA/SNAP, 2017). A Lee Sigma filter option was applied to the clipped images to address speckle effects (Lee et al., 1994). The filter had a 3 by 3 target window to limit the loss of image detail.

Subsequently, a two-stage classification was applied to determine river flood extent (Fig. 2, Parts 1a and 1b). Part 1a uses grey-level thresholding, which has been used in the development of flood mapping

algorithms in prior research (e.g. Giustarini et al., 2013; Long et al., 2014; Lu et al., 2014; Martinis et al., 2009; Matgen et al., 2007, 2011). Grey-level thresholding examines a histogram with a SAR image's pixel intensity/backscatter values on the x-axis (y-axis is the frequency count). In images with a high percentage of water, areas of land and water have distinctly separate histogram distributions. Smooth water is characteristically dark in SAR imagery as it is specularly reflected (Fig. 5). By contrast, rougher vegetation and land cover scatters a greater proportion of the original radar pulse back to the satellite sensor and thus appears brighter in the SAR image. Grey-level thresholding attempts to isolate the water pixels within a SAR image by defining the water distribution, but as water and land distributions frequently overlap this proves difficult. Prior research used the local minima value between the land-water distributions as the limiting value for water, but this tends to under-detect water. Therefore supplementary methods, such as change detection and region growing techniques (Giustarini et al., 2013; Long et al., 2014), have been used to successfully refine the water threshold value and improve classification of water pixels. This moves the threshold value upwards to include more of the (obscured) tail of the water distribution.

In this study, the procedure proposed by Matgen et al. (2011) was followed. Although the threshold was determined using an Extreme Value fitting tool in MATLAB (Statistics and Machine Learning toolbox) rather than using a gamma distribution fitting algorithm, as in this case it provided a closer fit to the water distribution. Values greater than the 99 percentile and less than the 1 percentile of this fit on the y-axis were removed, to eliminate the infinitely small values, and the resulting distribution was then rescaled to unity on the y-axis. We found the x-axis (backscatter, dB) value corresponding with the 0.01 (1%) y-axis
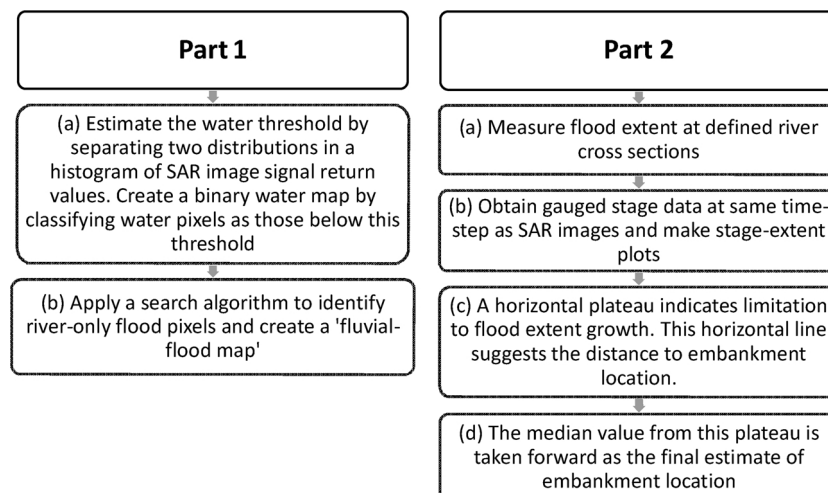
Fig. 2. Schematic showing key steps within the methodology.

value of the fitted distribution consistently provided a good estimate of water threshold. The water map generated using this estimate also compared well visually with the flood extent projected using flood levels measured against DEM data.

Using this grey-level thresholding method, the threshold estimate was 0.0154 dB for the One Hundred Foot Wash and 0.0061 dB for the Yolo Bypass. The method mimics the approach of the current radiometric thresholding research in this area and is also easily automated and reproducible. Nevertheless, a different y-axis percentage could be selected as appropriate to the data, or part 1a of the methodology can be replaced entirely with an alternative method for obtaining the water map.

2.1.2. Creating fluvial flood maps

For embankment detection, only the area inundated by river water is of interest. Water from ponding were removed from the initial binary water map to create a so-called fluvial flood map. We used a spread operation to create a fluvial flood map for part 1b, which was initiated at the river centre. We drew the river centre line manually in this study, but this could equally be derived from databases like HydroSHEDS (Lehner et al., 2008), or the Global-scale Width Database for Large Rivers (GWD-LR; Yamazaki et al., 2014). The operation works by spreading outwards from pixels representing the river centre line until a 'not-water' pixel is detected in one of eight cardinal directions. This halts the outward spread of the operation in that direction. Any water pixels beyond this void are identified as water pixels not obviously originating from the main river. The assumptions made here concerning flood pixel connectivity highlights the importance of defining the river line location as precisely as possible, and locating an appropriate intensity threshold for water in the SAR images as over- or under-detection of water pixels would also limit the spread operation.

2.2. Part 2: embankment location from stage-extent plots

Plateaus in the stage-extent plots (Fig. 1) indicate the embankment location. Although discharge data could equally be plotted against extent, in place of stage, we only present stage-extent plots for the sake of consistency here. To prepare stage-extent plots, cross sections were generated perpendicular to the river's axis (Fig. 2, 2a). The fluvial flood maps are rasters with the same pixel size as the original SAR data; flood extent was measured between river centre pixels and flood edge pixels on river left and river right. The flood edge is represented by the furthest water pixel away from the river centre line, along the cross section.

The measure of flood extent from a SAR image at a particular time-step is then plotted against stage level for the same time-step. This is repeated for all available SAR imagery in the time sequence, with stage on the x-axis and flood extent on the y-axis (Fig. 1b). A plot is made for each cross section. It was necessary to order the stage by increasing magnitude rather than by date order because during a single flood, stage does not just smoothly rise (and fall) through time (Fig. 4)

Each cross section stage-extent plot was visually examined for the appearance of a prolonged horizontal plateau (Fig. 1, 2(2c)). This is the extent value, i.e. distance from the river's axis, at which the embankment is predicted. Specifically, we used the median extent of all points comprising the plateau (Fig. 2(2d)) as the predictor of embankment location.

2.3. Positional error of the embankment location

We used reference data on the embankment location to compute the positional error of the predicted embankment location for validation purposes. The positional error was calculated (1) as the absolute error between the predicted embankment location and the reference location in metres along each cross section, and (2) as the median absolute error (MAE) over all cross sections at each test site. MAE was used because

errors were varying and mean results became considerably skewed as a result of some large outliers. Embankment reference locations were derived from LiDAR data, or ready-made geodatabases with embankment data (see Section 3.2).

To explain the positional errors of the embankment, the land cover and terrain height were examined for each cross section. High grounds limit flooding at low magnitude floods whereas emergent vegetation limits the detection of inundated floodplains as the SAR picks up the vegetation signal rather than the inundation signal. The along-cross-section length of vegetation and high ground was measured visually using georeferenced TerraColor maps and Google Maps in addition to the LiDAR data.

2.4. Sensitivity of embankment positional error to SAR threshold

The binary water map and the associated fluvial flood map depend strongly on the selected water threshold value in the SAR imagery. Therefore, we tested the method with a range of threshold values and evaluated the positional error as a function of the selected threshold. The positional error presented in this sensitivity test are given as the *signed* error, rather than absolute error, to highlight any under- or over-estimation of the embankment location.

Part 1 and Part 2 of the methodology were applied with a range of threshold values, varying ± 0.01 around the original water threshold in 0.0005 dB increments. Although all cross sections were tested, only the results from the cross section nearest to the gauge are presented. Due to fluctuations in error results between neighbouring threshold values, smoothing (Savitzky – Golay filter; Eilers, 2003) was applied for better visualisation in Fig. 9.

3. Data

The data used in this methodology are presented, including specifics of test locations, the hydrology and satellite data.

3.1. Test locations

The methodology was tested at two locations, chosen because they experienced recent flooding identifiable within time series of SAR data, had readily available hydrology and had known reference data. The study locations are similar in that the areas of interest are low lying and designed to accept diverted water from nearby watercourses during flood conditions. Multiple rivers and drainage channels are present and there is hydrological complexity added from downstream tidal influences at both locations. Both areas were designed for diversion and containment of flood waters by use of earth-filled embankments. They are however differentiated by domain size and volume of flood water inundation.

The first test location is at the One Hundred Foot Wash, off the Great Ouse River, located across the Norfolk/Cambridge county boundary in the UK (Fig. 3a). The flood detention basin is located within a low lying area prone to seasonal flooding and tidal incursion (Edwards, 2016), leading to saturated conditions in some areas. The 33 km long basin has the River Delph on the north-eastern section and the New Bedford River fringing the southern side. Flood waters regularly inundate during the winter months (Edwards, 2016). The One Hundred Foot Wash basin varies in width between approximately 230 m and 950m.

The second study location is the considerably larger network of the Yolo Bypass, located west of the city of Sacramento California, US. The bypass lies immediately adjacent to the Sacramento River; between the Freemont Weir and Rio Vista (Fig. 3b). The Bypass is approximately 60 km long and ranges between approximately 2.5 km and 8 km in width and is surrounded by new wetland and rice fields (Aquatic Science Center, 2012).
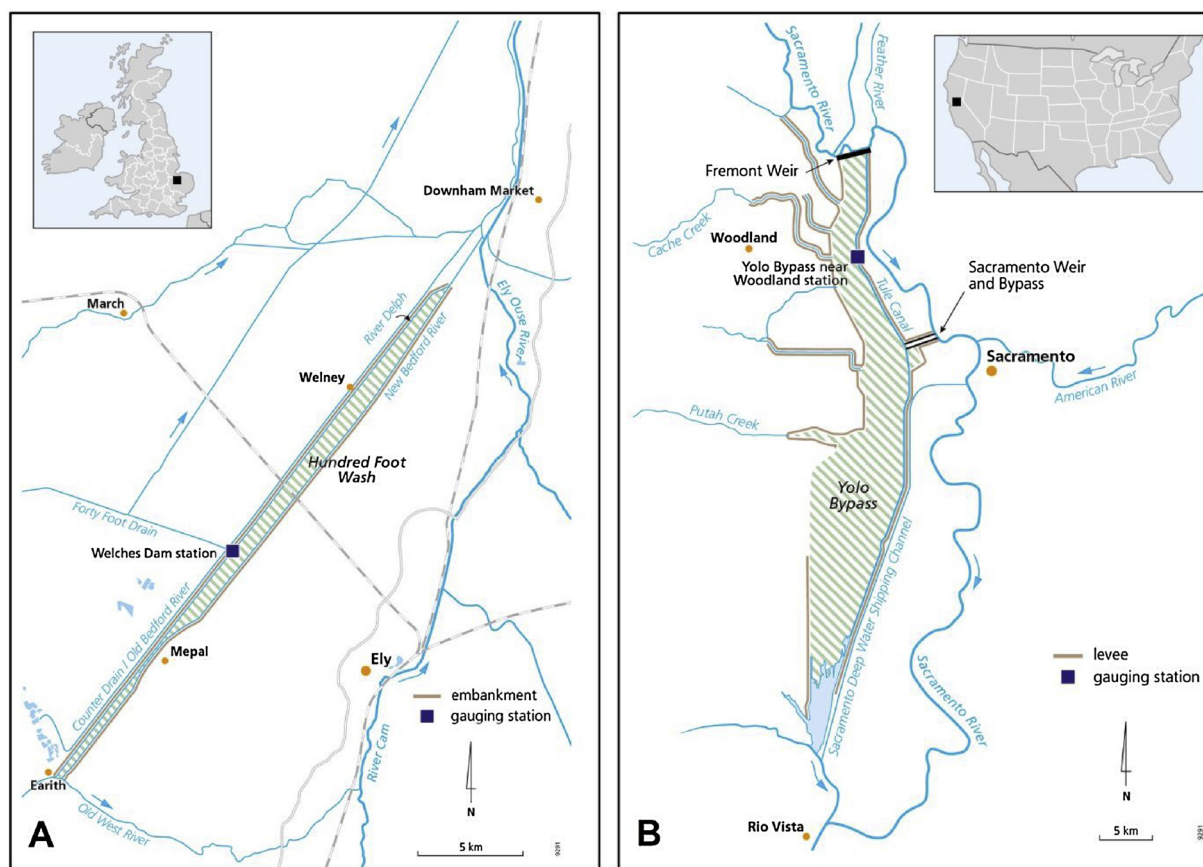
Fig. 3. A) A schematic of the One Hundred Foot Wash (based on Edwards, 2016). B) A schematic of the Yolo Bypass, Sacramento, California, USA. (based on California Department of Water Resources, 2017).

3.2. Hydrology and embankment reference data

The area around the One Hundred Foot Wash has a complex network of drainage channels, locks, weirs, sluice gates and pumping stations to drain the land. Level data for the gauging station utilised in this study was obtained from the Environment Agency of England and Wales (EA). Welches Dam station (Fig. 3a) is located at the centre of the One Hundred Foot Wash, inside the basin on the River Delph (station ID L33816). Stage data, expressed as metres Above Ordnance Datum (mAOD), were available from Welches Dam station between 2000 to 2016.

Stage data for the Yolo Bypass (Yolo Bypass nr. Woodland; station ID USGS 11453000) was obtained from the US Geological Survey National Water Information System (USGS, 2017). This station is on the Tule canal located within the bypass channel (Fig. 3b). It is hydraulically connected to the Sacramento River at high flows. Flows chiefly enter the Yolo Bypass from the Feather from the north and Sacramento Rivers and Cache Creek from the west, but numerous smaller channels and creeks also contribute, before draining southwards towards the Suisun and San Francisco Bays. Hydrographs for the study areas (Fig. 4) illustrate the peaks and timings of interest, with satellite acquisition times superimposed (red vertical lines). The stage information was extracted for the date and closest time of each satellite overpass.

Embankment reference data were derived from several sources. For the One Hundred Foot Wash, free-to-download LiDAR data at 2 m resolution (EA, 2017) were used to determine the reference embankment locations. For the full extent of the Yolo Bypass the national local levee database was available as a raster layer (USACE, 2017). The levee crown data were used for location validation in the methodology. Additional LiDAR data were at 3 m and 10 m resolution (NOAA, 2017 and USGS/NED, 2017 respectively), but these data were patchy throughout the domain and so was only used as ancillary validation data for visual inspection.

3.3. Sentinel 1 SAR data

SAR data products from the Sentinel-1 constellation were obtained from the dedicated Sentinel open access hub of the European Space Agency (ESA; ESA/Copernicus, 2017). The instruments on board the Sentinel-1 constellation of satellites use C-band radar frequencies (5.405 GHz; approximately 5.55 cm wavelength). Revisit times depends on location and latitude and vary between 1 (polar) and 3 (equator) days (~2 days for Europe). Level-1 Interferometric Wide (IW) Swath Mode high resolution Ground Range Detected (GRD) data were downloaded for this study. GRD data are projected to ground range using an Earth ellipsoid model. These data have a pixel spacing of 10 m × 10 m and a spatial resolution of 20 m (range) and 22 m (azimuth).

For the 70.5 km × 44 km area covering the One Hundred Foot Wash, there were 12 (dual VV-HV polarisation) complete Sentinel-1A images of the winter 2015 flood event; dated between 18 October 2015 and 25 March 2016 (Fig. 4a). There were 18 Sentinel-1A and −1B images of the Yolo Bypass obtained between 20 December 2016 and 24 February 2017 to cover the period of the developing flood and the preceding low flow state (Fig. 4b). A mixture of dual VV-HV and single VV polarisation data were obtained for the 188 km × 128 km Bypass area.

4. Results

Inundated areas show up in strong contrast during floods, compared to low flow conditions (Fig. 5). SAR images of the One Hundred Foot
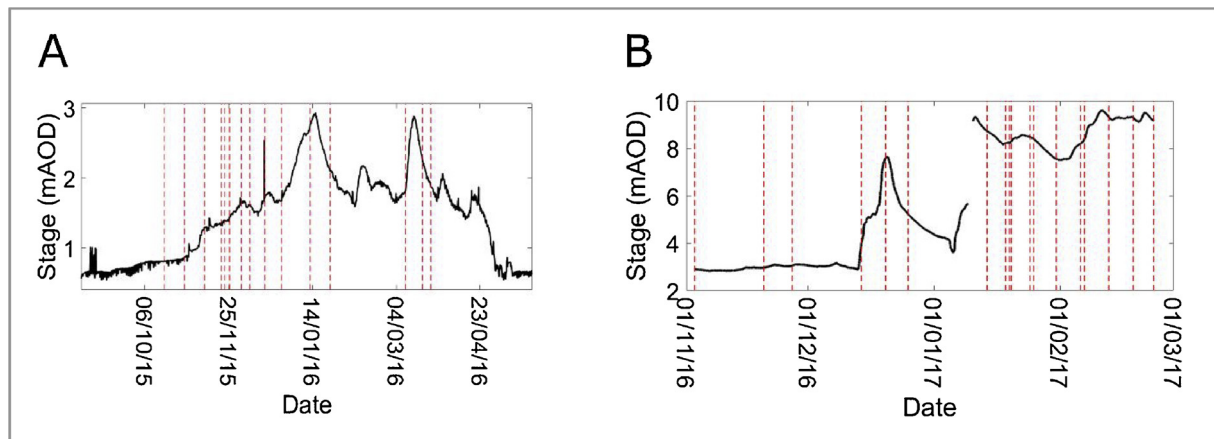
Fig. 4. Hydrographs for Welches Dam, River Delph (A) and Yolo Bypass (B). SAR observation dates are marked as red vertical lines. (For interpretation of the references to colour in this figure legend, the reader is referred to the web version of this article.)

Wash (Fig. 5a, b) and Yolo Bypass (Fig. 5c, d) in flood illustrate the contrast of water as dark pixels, where the proportion of reflected radar signal returning to the satellite sensor is negligible. We present here the predicted embankment location according to the methodology, the validation and the sensitivity.

4.1. Location prediction

The stage-extent plot for the cross section nearest to the Welches Dam (Fig. 6a) exemplifies the cross sections of the One Hundred Foot Wash. It shows a step-change in flood extent as water levels rise out of the channel and fill the floodplain. This is most evident for the right-of-channel flood extent is at between 1.5mAOD and 1.6mAOD. After 1.65mAOD a horizontal plateau forms. The distance to the right side embankment position was calculated as the median flood extent value of the horizontal plateau when stage exceeds 1.6mAOD, giving a predicted location of 826 m along-cross-section distance. Validation shows the absolute error was 42 m (approximately two Sentinel-1 pixels) for this cross section.

Left-of-channel flood extent for the same cross section was small since the river abuts the embankment, although a noisy horizontal plateau is nevertheless evident in Fig. 6a. The plateau indicates a median predicted distance to embankment of 64 m (an absolute error of 36 m) for this cross section. The single observation of ~650 m flood extent at water level 2.2 m is isolated and could be a misdetection due to saturated soil or an overestimate of the water threshold in a single SAR image. The MAE over all nine cross sections, including both sides

of the river axis, was 78m. Four cross sections contained more than 100 m continuous length of either high ground or emergent vegetation. With these sections excluded, the MAE of all One Hundred Foot Wash cross sections decreased to 59 m.

The stage-extent plot for the Yolo Bypass (Fig. 6b) represents the cross section 2.59 km upstream of the gauging station. It shows an emphatic incline to indicate expanding flood extent just before a horizontal plateau occurs. In this instance, the median plateau value estimates the levees to be located a distance of around 953 m (left levee; median of stage over 7mAOD) and 1596 m (right levee; median of stage over 7mAOD). The levee position was underestimated with an absolute error of 110 m on the left levee and 60 m on the right levee. The MAE over the 13 cross sections and two river sides was 197 m. But this decreases to a MAE of 110 m when cross sections with more than 100 m length of vegetation, or high ground were excluded.

The predicted embankment locations in Fig. 7 illustrate the position and the associated error for all extracted embankment points for both study areas. The markers are superimposed on Sentinel GRD product, for the One Hundred Foot Wash (Fig. 7a) and Yolo Bypass (Fig. 7b) locations. The embankment reference locations are indicated as a purple lines, which represent the embankment crowns. When considering all cross sections, not just those upstream of the gauge, the prediction errors range between 22 m and 700 m.

Examination of the terrain height and emergent vegetation in relation to the prediction error (Fig. 8) revealed that the largest errors were due to ground being higher than local stage levels preventing the full expansion of the water up to the embankments. Examination of the
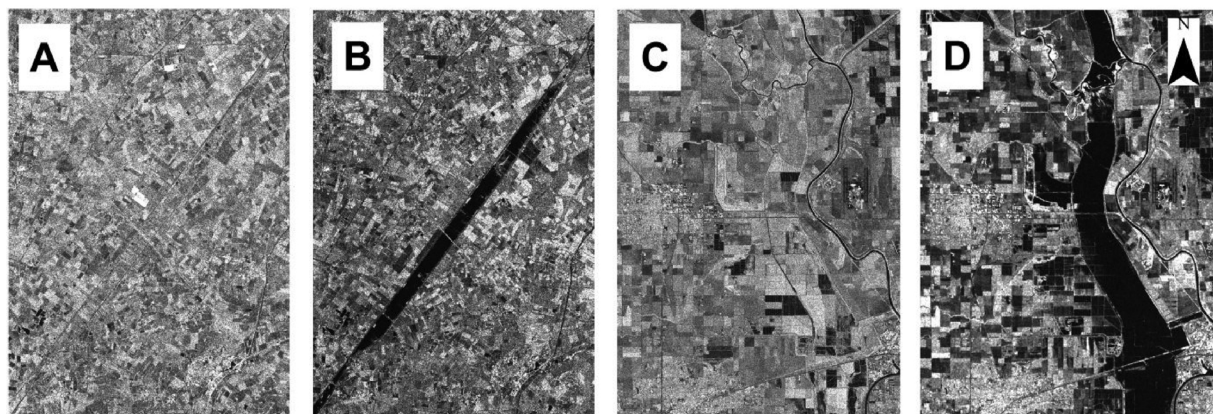

Fig. 5. Multi-temporal Sentinel-1 SAR data. The One Hundred Foot Wash of 30th October 2015 before the flood event (A) and during the flood on 10th March 2016. Yolo Bypass on 20th November 2016 before the flood event (C) and during the flood on 24th February 2017.
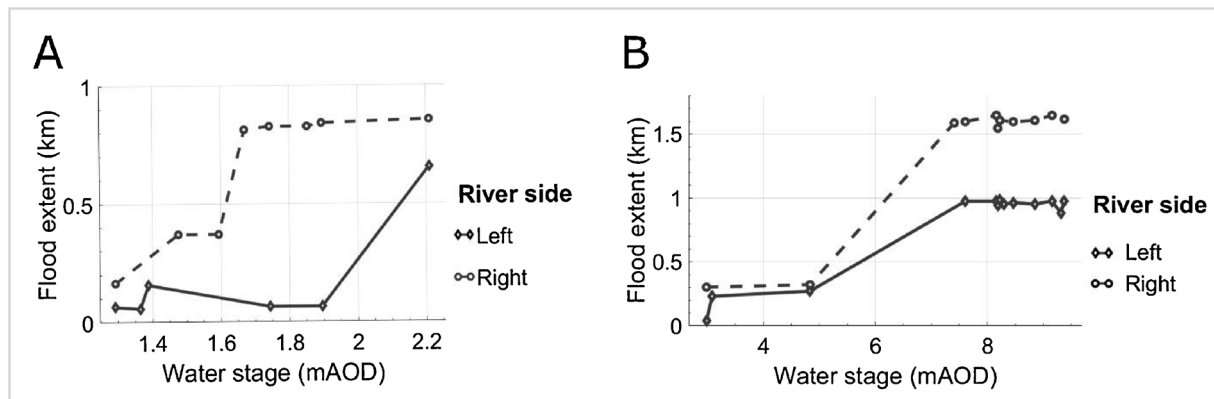
Fig. 6. A) One Hundred Foot Wash stage-extent plot for the cross section upstream of gauge. B) Yolo Bypass stage-extent plot for the cross section upstream of gauge. Each marker plotted represents one Sentinel-1 observation of flood extent.

hydrology (Fig. 4) shows the flood events were not exceptionally large and therefore, for some cross sections, the flood height was insufficient to reach the embankments. Additionally, Fig. 8 shows that a consistent cause of underestimation is due to vegetation, the amount of which varies according to the cross section. Vegetation (indicated green) is most evident in the Yolo Bypass (Fig. 8b) compared to the One Hundred Foot Wash (Fig. 8a). The errors labelled as 'Other' can be attributed to the methodology itself or to measurement errors.

4.2. Sensitivity analysis

The water threshold value was used to create the binary water map (Fig. 2, Part 1a) and consequently for determining the fluvial flood map and the associated embankment location. For this sensitivity test, the threshold value was varied ± 0.01 dB around the original water threshold estimate (as established in Section 2.1.1) in 0.0005 dB increments.

Fig. 9 shows the results of this analysis, with the difference between observed and predicted flood extent expressed as signed error for the
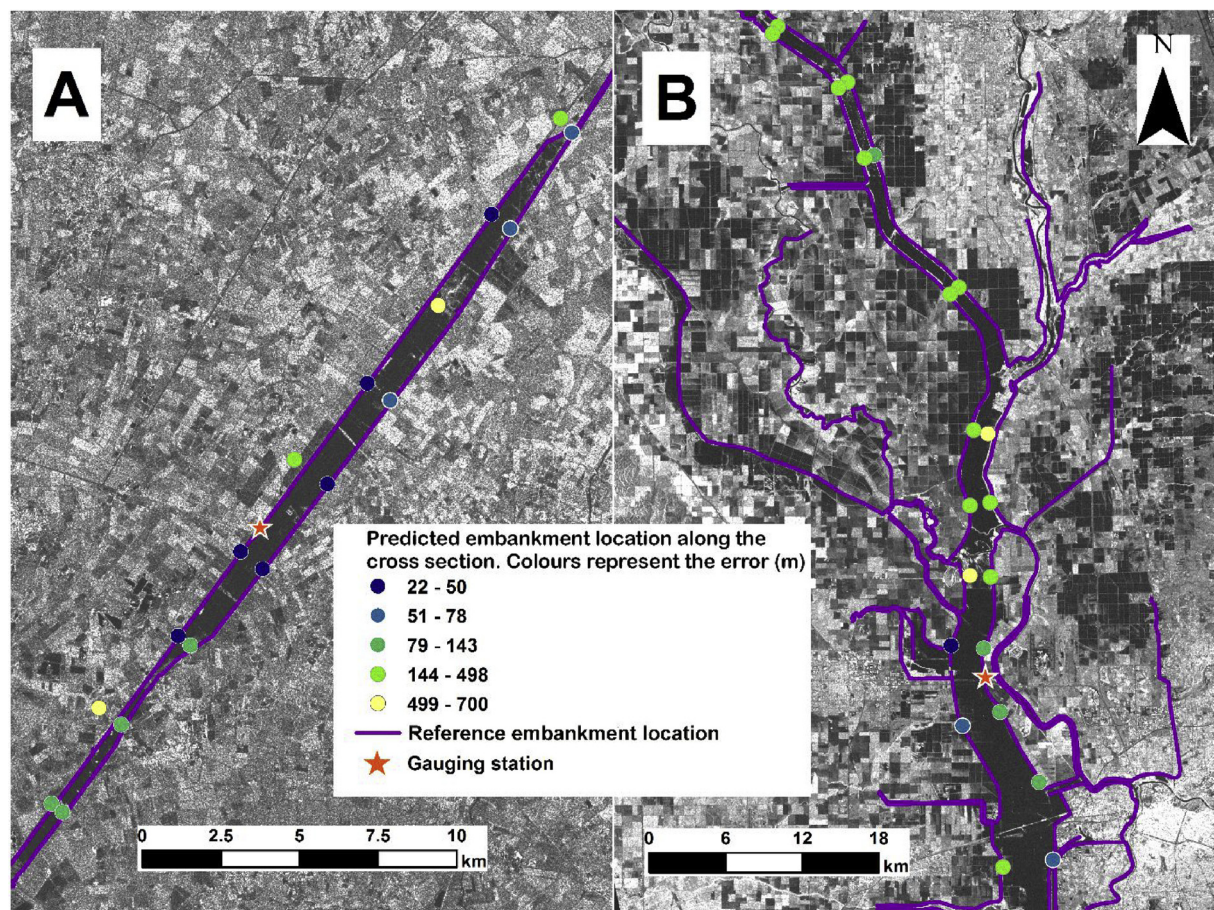

Fig. 7. Predicted embankment locations from time series of SAR data and gauge data. The circles represent the extracted embankment points along the cross sections and the colours of each circle represent the positional error relative to the reference embankment. A) the One Hundred Foot Wash, UK, and (B) Yolo Bypass, Sacramento, USA. (For interpretation of the references to colour in this figure legend, the reader is referred to the web version of this article.)
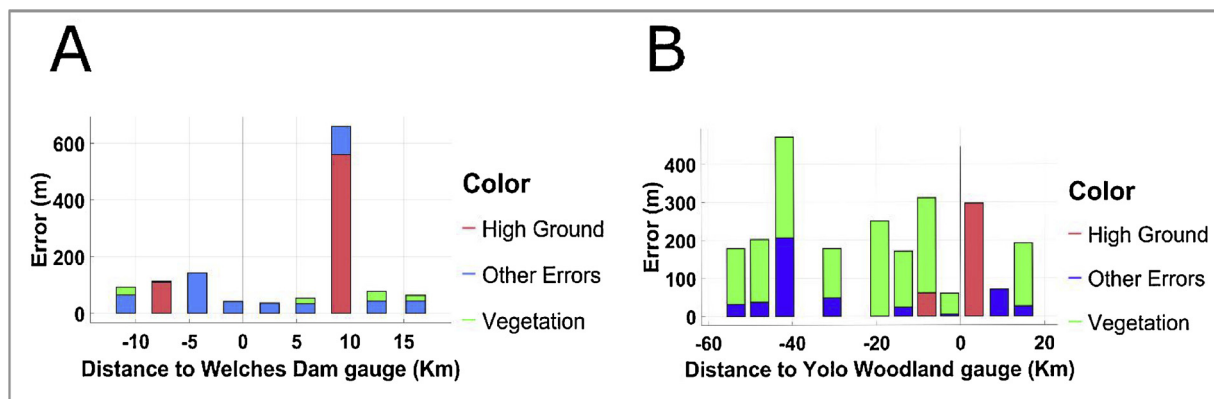
Fig. 8. Source of underestimation errors for A) One Hundred Foot Wash (right-of-channel errors only) and B) Yolo Bypass (both sides of channel). (For interpretation of the references to colour in this figure legend, the reader is referred to the web version of this article.)

cross section 0.9 km upstream of the River Delph gauge (Fig. 9a), and 2.59 km upstream of the Yolo Bypass gauge (Fig. 9b). Left and right of channel results are combined in each plot. The shaded zones in each figure indicate the extent of uncertainty (with penalized least squares method in MATLAB: Eilers, 2003).

The signed error shows a clear optimum signal return value to define flood extent in each location, though this value is not the same one for each case study location. For the One Hundred Foot Wash (Fig. 9a), a water threshold value of between approximately 0.013 dB and 0.018 dB provides smallest error in determining flood embankment location at the chosen cross section. For the Yolo Bypass, a threshold between 0.0025 dB and 0.0075 dB provides closest to zero error in determining flood levee location, at the chosen cross section. In both case study locations, with higher or lower threshold values than the optimum, the kilometre error can be substantial.

Overall, the result for this single cross section (which it is assumed holds for all cross sections within the domain) shows a high sensitivity to choice of water threshold value. But notably, the methodology outlined in section 2.1.1 did successfully determine a value within the optimal range (i.e. 0.0154 dB for the One Hundred Foot Wash and 0.0061 dB for the Yolo Bypass).

5. Discussion

The aim of this paper was to develop a methodology for locating flood embankments using SAR data combined with local gauge data and estimate the positional accuracy of the methodology using reference data. The previous section presented results and considered the

sources of any errors that occurred. The implication of these results are discussed below.

5.1. Locating flood defences

The methodology has been shown to work well for both test locations within this study, even though flood levels were not yet approaching the top of the embankments to indicate precise location. To improve the precision of embankment mapping, the availability of a longer time series of images, covering more extreme flood events, would be beneficial. The results also showed errors ranging between 22 m and 700 m. With a Sentinel-1 spatial resolution of 20 m × 22 m, the method can be accurate under ideal conditions to within 1–3 pixels. Larger errors could be ascribed to not only insufficiently high water levels but also to the presence of vegetation at flood edges. The presence of vegetation is a well-known problem in detecting the exact flood edge with SAR sensors (Horritt et al., 2003; Martinis et al., 2009; Mason et al., 2014) and it significantly contributed to the under-detection of flood embankment location in this study. Past research in defining water edge using ~30 m spatial resolution ERS SAR data, which did not always suffer the same vegetation problem, had a mean error of between approximately 65 m and 120 m (Dellepiane et al., 2004; Horritt et al., 2003; Niedermeier et al., 2000). For all cross sections generated within the One Hundred Foot Wash the median absolute error (MAE) was 78 m, and for the Yolo Bypass the MAE was 197 m. MAE were reduced substantially for both locations when cross sections with obvious (> 100 m continuous length) vegetation or high ground were removed from the sample: MAE for the One Hundred Foot Wash
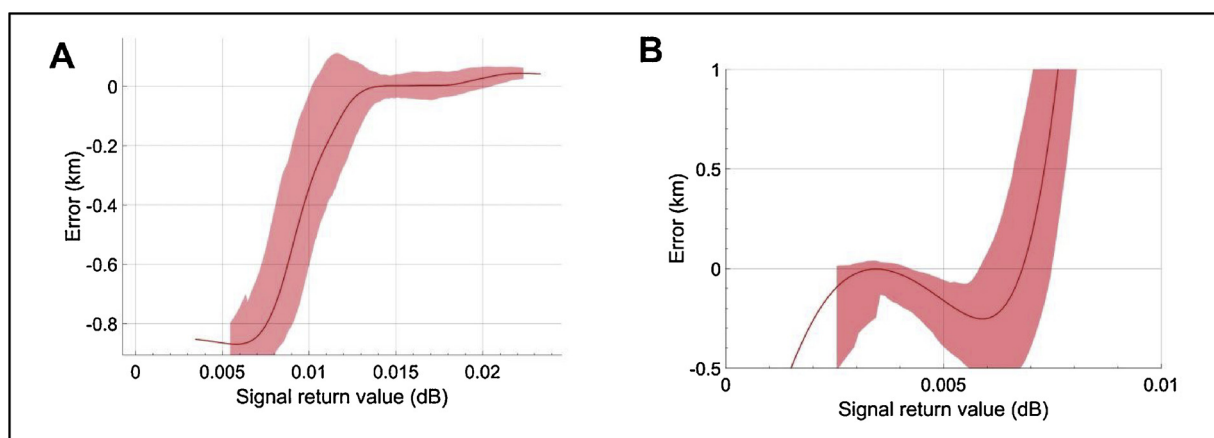
Fig. 9. Sensitivity of the error in flood defence detection, through varying 'water-threshold' values. For A) the River Delph, One Hundred Foot Wash, Cambridgeshire and B) the Yolo Bypass, Sacramento, California. Error is signed error (km). Zero crossing on the y-axis represents the optimum signal return value.
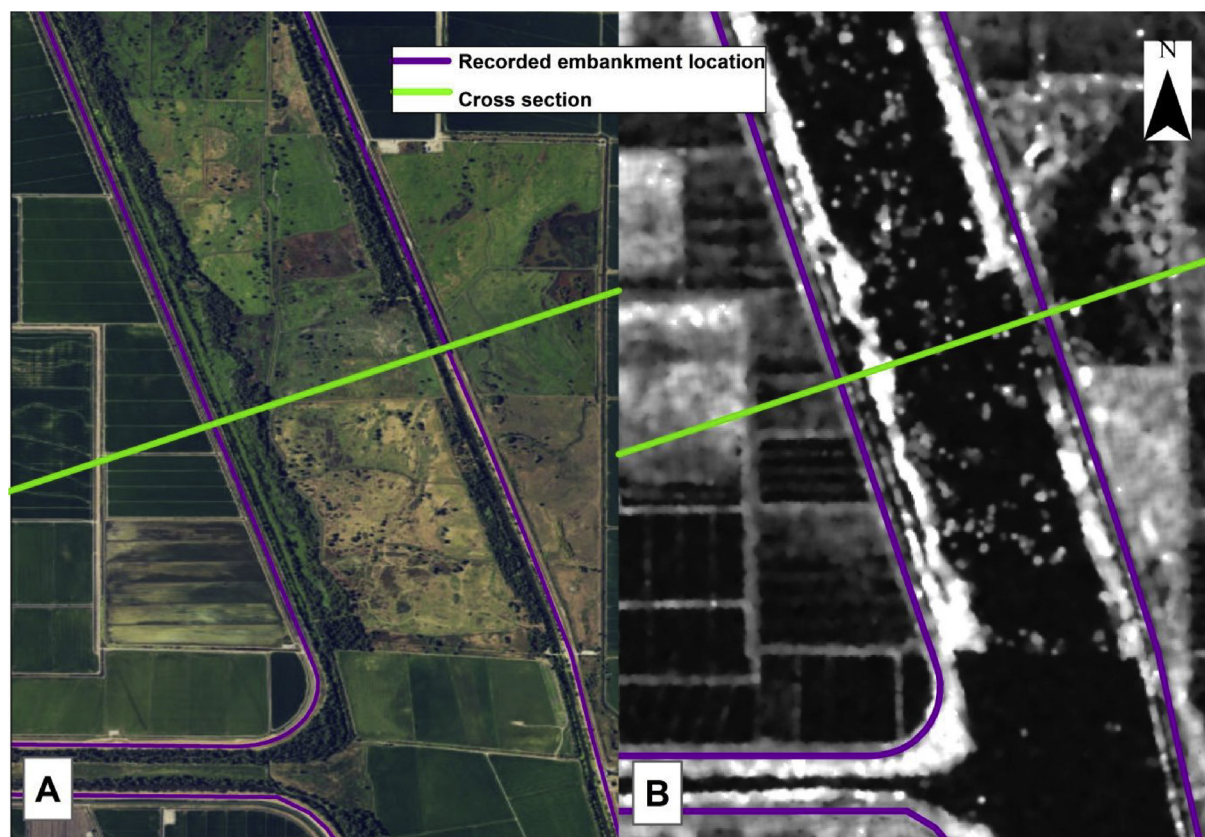
Fig. 10. A) TerraColor image (source: Esri, Digitalglobe, GeoEye, Earthstar Geographics) of the Yolo Bypass. B) The same scene observed by Sentinel-1 satellite (ESA) on 24th February 2017 showing full flood extent and signal scatter due to vegetation along the embankments. (For interpretation of the references to colour in this figure legend, the reader is referred to the web version of this article.)

reduced to 59 m and MAE for the Yolo Bypass reduced to 110m.

Fig. 10 illustrates a typical scene for the Yolo Bypass with cross sections (green) and levee (purple) marked. On the left (Fig. 10a) is a non-flood optical image and on the right (Fig. 10b) is the same scene, in-flood, as observed by SAR satellite. Dark pixels in Fig. 10b represent water and the white areas indicate the scatter of the radar signal from trees, brush and emergent vegetation, which are obscuring the flood edge adjacent to the embankments.

New wetland and rice cultivation around the Yolo bypass are also evident in Fig. 10, which illustrates the potential for detection errors associated with the choice of water threshold value. The binary water maps cannot always easily discriminate between saturated soil/emergent vegetation signatures and open water. Where there is a greater depth of water present (e.g. the One Hundred Foot Wash right-side flood extent, Fig. 6a), the difference between water and not-water pixels is obvious. But for areas where vegetation and shallow water blend, such as wetland areas and the flood boundary fringes, there is difficulty determining the water threshold value precisely as the signal texture is a combination of both rough and smooth surfaces.

The creation of the fluvial flood map from the binary water map becomes especially challenging if the flood edge location is also uncertain (e.g. the One Hundred Foot Wash left-side flood extent, Fig. 6a). We used a relatively simple spread operation to map the provenance of the water, and this could be refined in future research. Application of statistical methods such as use of fuzzy logic (Pulvirenti et al., 2011), split-based automation (Martinis et al., 2009) or active contour models (Horritt et al., 2001; Horritt, 1999) could be beneficial for more effective discrimination between neighbouring pixels. Also the research in cross polarisation, and using phase data to decompose backscatter into types (Henry et al., 2006; Manjusree et al., 2012), curvelet-based change detection (Schmitt et al., 2014; White et al., 2015), InSAR

coherence (Pulvirenti et al., 2016; Refice et al., 2014) and incidence angle (Manjusree et al., 2012) are some areas of research that could provide new insights to further improve Part 1b – the creation of fluvial flood maps – with SAR imagery. Automatic flood map creation is already available with online tools (e.g. ESA's Grid Processing on Demand service; Westerhoff et al., 2013; Giustarini et al., 2016).

Spatial resolution may also affect the accuracy of embankment positioning. Indicative plateauing was not found in the stage-extent plots for some cross sections (e.g. One Hundred Foot Wash, left-of-channel: Fig. 6a). This could simply be due to water levels not yet reaching a structure, or it could be a result of the pixel resolution. The toe to toe average width of the left side embankment in the One Hundred Foot Wash is approximately 26 m and Sentinel-1 satellite data have a spatial resolution of 20 m. Therefore it is possible in this case that the embankments are on the limits to be resolved under circumstances where water is detected on both sides of the structure.

Temporal considerations are also important as the key flood extents must be captured. Ideally, the SAR sequence should observe the flood approaching not just the embankment toe but the crown height as well, should the magnitude of flooding be severe enough. The timing between SAR acquisitions is only important in that the sequence should capture the flood development – this would for example present a limitation for observing fast-developing floods (e.g. steep, modified or small catchments). For this study, the hydrographs with overlaid SAR acquisition times (Fig. 4) show that the development of a moderate sized flood was well captured for the test locations but embankments were not overtopped.

5.2. Standards of flood defence

The objectives of this study were limited to proving that it is

possible to locate flood embankments, using a sequence of SAR data with hydrology, with an indication of the obtained accuracy. A future use of this methodology however would be to estimate embankment height and flood protection standard using the link between gauge data and observed flood extent. The critical data would be an observation sequence including full-to-embankment-crown flooding. In concept, this is indicated by a long horizontal plateau ending in a sharp vertical climb (Fig. 1b). This did not occur in the data in this study, nevertheless minimum flood protection standards can still be inferred from the stage levels.

5.3. Sensitivity testing

The methodology outlined in section 2 utilises a curve fitting procedure to approximate the water threshold of a SAR image, as a preliminary to the creation of fluvial flood maps for each location. Yet the threshold selection is an estimate and where the radiometric segmentation and interpretation is complex – such as where water and land are observed together – it may actually be a source of error in the final determination of embankment location.

The outcome of the sensitivity testing showed that the techniques used placed the estimated threshold value within an optimal range at both locations, and that small variations of ± 0.001 dB would not significantly alter flood extent. While the estimate for the Yolo Bypass was good, the methodology did slightly overestimate the threshold value, resulting in a slight overestimation of flood extent in this test. Therefore more scrutiny on water pixel classification in the initial stages of the methodology could act to improve final results.

However classification errors arise not only from radiometric thresholding technique. Speckle filters on the SAR data products use spatial averaging which could reduce the image resolution and affect the accuracy of the final result. Shadow or bounce effects also contribute to classification errors generally, although the test sites are deliberately located in flat and comparatively featureless areas.

6. Conclusions

Hydrodynamic models and flood management strategies frequently lack suitable data on embankment location and height, as it difficult to collect for reasons of location, scale or cost. This paper presents a new methodology to estimate the location of flood embankments using only a sequence of SAR imagery and gauge data. Uniquely, no topographic data are needed.

The semi-automated methodology successfully located flood embankments at case study locations in the UK and USA. While there can be errors in detecting food embankment location if the full flood extent is limited (e.g. from low water levels or high land) or where the SAR image signal value is difficult to resolve or classify (e.g. water threshold issues), the largest source of error was due to vegetation obscuring the true flood edge. There is therefore potential to reduce errors significantly if vegetated cross sections are excluded, i.e. avoid locating cross sections on top of bright signal returns in a SAR image. When this was done here the MAE of locating embankments reduced from underestimates of 78 m and 197 m to 59 m and 110 m, in the One Hundred Foot Wash and Yolo Bypass locations, respectively.

This analysis suggests the methodology can be further improved by focussing on image processing, particularly in detecting flood edge where there is vegetation present. Spatial resolution may also limit detection of narrow embankments, where flood extent is small, or where there are complex signal returns around saturated ground. Therefore future work to improve the method could focus on refining the procedures for obtaining fluvial flood maps such as (1) improving pixel classification methods (or to utilise a reliable online web-service, such as ESA's upcoming Grid Processing on Demand service for Sentinel-1 data); and (2) reducing error from vegetation and high ground. Optimising the sampling frequency of observations could also

streamline the creation of the stage-extent plots. Indeed, if a time series of SAR images were to capture an extreme flood event – up to the embankment crown maxima – there is also potential for the methodology to capture key information on embankment protection heights and defence standards.

The ultimate ambition for this methodology would be to use it in ungauged locations (i.e. relying solely on SAR observations to detect flood embankments and no longer using gauged data), therefore future work could be to test it with modelled or statistically-derived flows at a point of interest. The embankment-locating methodology presented here therefore has the potential for global application, and could provide critical information for hydrodynamic models and existing river databases.

References

Alfieri, L., Burek, P., Dutra, E., Krzeminski, B., Muraro, D., Thielen, J., Pappenberger, F., 2013. GloFAS-global ensemble streamflow forecasting and flood early warning. Hydrol. Earth Syst. Sci. 17 (3), 1161.

Alfieri, L., Bisselink, B., Dottori, F., Naumann, G., Roo, A., Salamon, P., Wyser, K., Feyen, L., 2017. Global projections of river flood risk in a warmer world. Earth's Future 5 (2), 171–182.

Aquatic Science Center, 2012. The Pulse of the Delta: Linking Science & Management Through Regional Monitoring. Contribution No. 673. Aquatic Science Center, Richmond, CA. http://www.aquaticscience.org.

Bates, P.D., 2012. Integrating remote sensing data with flood inundation models: how far have we got? Hydrol. Processes 26 (16), 2515–2521.

Biggin, D.S., Blyth, K., 1996. A comparison of ERS-1 satellite radar and aerial photography for river flood mapping. J. Chart. Inst. Water Environ. Manage. 10, 59–64.

Blom, R.G., Crippen, R.E., Elachi, C., 1984. Detection of subsurface features in SEASAT radar images of Means Valley, Mojave Desert, California. Geology 12 (6), 346–349.

Briese, C., 2004. Three-dimensional modelling of breaklines from airborne laser scanner data. Int. Arch. Photogram. Remote Sens. Spat. Inf. Sci. 35 (Part B/3), 1097–1102.

California Department of Water Resources, 2017. A Schematic Map of the Yolo Bypass. (Accessed 7 June at: http://www.water.ca.gov/aes/yolo).

Carvajal, F., Agüera, F., Pérez, M., 2011. Surveying a landslide in a road embankment using unmanned aerial vehicle photogrammetry. International Conference on Unmanned Aerial Vehicle in Geomatics (UAV-g). pp. 14–16.

Chang, L., Dollevoet, R., Hanssen, R.F., 2014. Railway infrastructure monitoring using satellite radar data. Int. J. Railway Technol. 3 (2), 79–91.

Czuba, Christiana, Byron, Williams, Jack, Westman, Keith, LeClaire, 2015. An Assessment of Two Methods for Identifying Undocumented Levees Using Remotely Sensed Data: U.S. Geological Survey Scientific Investigations Report 2015–5009. http://dx.doi.org/10.3133/sir20155009. 19 p., ISSN 2328-0328 (online).

Dabbiru, L., Aanstoos, J.V., Younan, N.H., 2014. Comparison of L-band and X-band polarimetric SAR data classification for screening earthen levees. In: 2014 IEEE Geoscience and Remote Sensing Symposium. July, IEEE. pp. 2723–2726.

Dellepiane, S., De Laurentiis, R., Giordano, F., 2004. Coastline extraction from SAR images and a method for the evaluation of the coastline precision. Pattern Recognit. Lett. 25 (13), 1461–1470.

Deutsch, M., Estes, J.E., 1980. Landsat detection of oil from natural seeps. Photogramm. Eng. Remote Sens. 46 (10), 1313–1322.

Di Baldassarre, G., Montanari, A., Lins, H., Koutsoyiannis, D., Brandimarte, L., Blöschl, G., 2010. Flood fatalities in Africa: from diagnosis to mitigation. Geophys. Res. Lett. 37, L22402. http://dx.doi.org/10.1029/2010GL045467.

EA, 2017. Environment Agency Geomatics Survey Data. (Web page, Accessed January 2017 at http://environment.data.gov.uk/ds/survey/#/survey).

EOPORTAL. Web page, Accessed 8 August 2017 at https://directory.eoportal.org.

ESA, 2013. Sentinel-1 User Handbook. Issue 1 Revision 0. GMES-S1OP-EOPG-TN-13-0001. Paris, France, European Space Agency.

ESA/Copernicus, 2017. Open Access Hub. (Web page, Accessed 30 May 2017 at https://scihub.copernicus.eu/).

ESA/SAR, 2017. Sentinel-1 SAR Technical Guide. (Web page, Accessed 30 May 2017 at https://sentinel.esa.int/web/sentinel/technical-guides/sentinel-1-sar).

ESA/SNAP. Version 5.0.0 available from web page, (Accessed 5 August 2017 at http://

step.esa.int/main/toolboxes/snap/).

Edwards, E., 2016. The Ouse Washes Website. (Accessed 7 June 2017 at http://www.ousewashes.info).

Eilers, P.H., 2003. A perfect smoother. Anal. Chem. 75 (14), 3631–3636.

Farr, T.G., Rosen, P.A., Caro, E., Crippen, R., Duren, R., Hensley, S., Kobrick, M., Paller, M., Rodriguez, E., Roth, L., Seal, D., 2007. The shuttle radar topography mission. Rev. Geophys. 45 (2).

Gang, W., Prinet, V., Feng, W., Songde, M., 2003. Dike detection using active contour model. Geoscience and Remote Sensing Symposium. In: July, IEEE. Proceedings. 2003 IEEE International, vol. 4. pp. 2523–2525 (IGARSS'03).

Giustarini, L., Hostache, R., Matgen, P., Schumann, G.J.P., Bates, P.D., Mason, D.C., 2013. A change detection approach to flood mapping in urban areas using TerraSAR-X. IEEE Trans. Geosci. Remote Sens. 51 (4), 2417–2430.

Giustarini, L., Hostache, R., Kavetski, D., Chini, M., Corato, G., Schlaffer, S., Matgen, P., 2016. Probabilistic flood mapping using synthetic aperture radar data. IEEE Trans. Geosci. Remote Sens. 54 (12), 6958–6969.

Google Maps (HFW), 2017a. Welches Dam, March, UK, Satellite Layer. (viewed 13 April 2017 https://www.google.nl/maps/@52.4818286,0.202233,7340m/data=!3m1!1e3).

Google Maps (Yolo), 2017b. Yolo Bypass, Sacramento, Satellite Layer. (viewed 4 April 2017 https://www.google.nl/maps/@38.6289135,-121.6623873,31674m/data=!3m1!1e3).

Gruen, A., Zhang, Z., Eisenbeiss, H., 2012. UAV photogrammetry in remote areas-3D modeling of Drapham Dzong, Bhutan. ISPRS -Int. Arch. Photogramm. Remote Sens. Spat. Inf. Sci B1.

Henry, J.B., Chastanet, P., Fellah, K., Desnos, Y.L., 2006. Envisat multi-polarized ASAR data for flood mapping. Int. J. Remote Sens. 27 (10), 1921–1929.

Herold, N.D., Haack, B.N., Solomon, E., 2004. An evaluation of radar texture for land use/cover extraction in varied landscapes. Int. J. Appl. Earth Obs. Geoinf. 5 (2), 113–128.

Hong, Y., Adler, R.F., Hossain, F., Curtis, S., Huffman, G.J., 2007. A first approach to global runoff simulation using satellite rainfall estimation. Water Resour. Res. 43, W08502. http://dx.doi.org/10.1029/2006WR005739.

Horritt, M.S., Mason, D.C., Luckman, A.J., 2001. Flood boundary delineation from synthetic aperture radar imagery using a statistical active contour model. Int. J. Remote Sens. 22 (13), 2489–2507.

Horritt, M.S., Mason, D.C., Cobby, D.M., Davenport, I.J., Bates, P.D., 2003. Waterline mapping in flooded vegetation from airborne SAR imagery. Remote Sens. Environ. 85 (3), 271–281.

Horritt, M., 1999. A statistical active contour model for SAR image segmentation. Image Vis. Comput. 17 (3), 213–224.

Horritt, M., 2006. A methodology for the validation of uncertain flood inundation models. J. Hydrol. 326 (1), 153–165.

Hostache, R., Matgen, P., Schumann, G., Puech, C., Hoffmann, L., Pfister, L., 2009. Water level estimation and reduction of hydraulic model calibration uncertainties using satellite SAR images of floods. IEEE Trans. Geosci. Remote Sens. 47 (2), 431–441.

Hu, C., Li, X., Pichel, W.G., Muller-Karger, F.E., 2009. Detection of natural oil slicks in the NW Gulf of Mexico using MODIS imagery. Geophys. Res. Lett. 36, L01604. http://dx.doi.org/10.1029/2008GL036119.

Imhoff, M.L., Vermillion, C., Story, M.H., Choudhury, A.M., Gafoor, A., Polcyn, F., 1987. Monsoon flood boundary delineation and damage assessment using space borne imaging radar and Landsat data. Photogramm. Eng. Remote Sens. 53 (4), 405–413.

Krüger, T., Meinel, G., 2008. Using Raster DTM for Dike Modelling. Advances in 3D Geoinformation Systems. pp. 101–113.

Krieger, G., Moreira, A., Fiedler, H., Werner, M., Younis, M., Zink, M., 2007. TanDEM-X: a satellite formation for high-resolution SAR interferometry. IEEE Trans. Geosci. Remote Sens. 45 (11), 3317.

Lai, X., Monnier, J., 2009. Assimilation of spatially distributed water levels into a shallow-water flood model. Part I: mathematical method and test case. J. Hydrol. 377 (1), 1–11.

Lee, J.S., Jurkevich, L., Dewaele, P., Wambacq, P., Oosterlinck, A., 1994. Speckle filtering of synthetic aperture radar images: a review. Remote Sens. Rev. 8 (4), 313–340.

Lehner, B., Verdin, K., Jarvis, A., 2008. New global hydrography derived from spaceborne elevation data. Trans. AGU 89 (10), 93. http://dx.doi.org/10.1029/2008EO100001.

Long, S., Fatoyinbo, T.E., Policelli, F., 2014. Flood extent mapping for Namibia using change detection and thresholding with SAR. Environ. Res. Lett. 9 (3), 035002.

Lu, J., Giustarini, L., Xiong, B., Zhao, L., Jiang, Y., Kuang, G., 2014. Automated flood detection with improved robustness and efficiency using multi-temporal SAR data. Remote Sens. Lett. 5 (3), 240–248.

Manjusree, P., Kumar, L.P., Bhatt, C.M., Rao, G.S., Bhanumurthy, V., 2012. Optimization of threshold ranges for rapid flood inundation mapping by evaluating backscatter profiles of high incidence angle SAR images. Int. J. Disaster Risk Sci. 3 (2), 113–122.

Marapareddy, R., Aanstoos, J.V., Younan, N.H., 2016. A supervised classification method for levee slide detection using complex synthetic aperture radar imagery. J. Imaging 2 (3), 26.

Martinis, S., Twele, A., Voigt, S., 2009. Towards operational near real-time flood detection using a split-based automatic thresholding procedure on high resolution TerraSAR-X data. Nat. Hazards Earth Syst. Sci. 9 (2), 303–314.

Mason, D.C., Davenport, I.J., 1996. Accurate and efficient determination of the shoreline in ERS-1 SAR images. IEEE Trans. Geosci. Remote Sens. 34 (5), 1243–1253.

Mason, D.C., Horritt, M.S., Dall'Amico, J.T., Scott, T.R., Bates, P.D., 2007. Improving river flood extent delineation from synthetic aperture radar using airborne laser altimetry. IEEE Trans. Geosci. Remote Sens. 45 (12), 3932–3943.

Mason, D.C., Speck, R., Devereux, B., Schumann, G.J.P., Neal, J.C., Bates, P.D., 2010. Flood detection in urban areas using TerraSAR-X. IEEE Trans. Geosci. Remote Sens. 48 (2), 882–894.

Mason, D., Garcia-Pintado, J., Dance, S., 2014. Improving flood inundation monitoring

and modelling using remotely sensed data. Civil Eng. Surv. 34–37.

Matgen, P., Schumann, G., Henry, J.B., Hoffmann, L., Pfister, L., 2007. Integration of SAR-derived river inundation areas, high-precision topographic data and a river flow model toward near real-time flood management. Int. J. Appl. Earth Obs. Geoinf. 9 (3), 247–263.

Matgen, P., Hostache, R., Schumann, G., Pfister, L., Hoffmann, L., Savenije, H.H.G., 2011. Towards an automatic SAR-based flood monitoring system. Lessons learned from two case studies. Phys. Chem. Earth 36 (7/8), 241–252.

Milillo, P., Tapete, D., Cigna, F., Perissin, D., Salzer, J., Lundgren, P., Fielding, E., Burgmann, R., Biondi, F., Milillo, G., Serio, C., 2016. Structural health monitoring of engineered structures using a space-borne synthetic aperture radar multi-temporal approach: from cultural heritage sites to war zones. SPIE Remote Sensing. International Society for Optics and Photonics (100030N-100030N).

Montanari, M., Hostache, R., Matgen, P., Schumann, G., Pfister, L., Hoffmann, L., 2009. Calibration and sequential updating of a coupled hydrologic-hydraulic model using remote sensing-derived water stages. Hydrol. Earth Syst. Sci. 13 (3), 367–380.

NOAA (National Oceanic and Atmospheric Administration), 2017. Digital Coast Data Access Viewer. Custom Processing of 1997 Sacramento Inland Floodplain Lidar (CA). NOAA Office for Coastal Management, Charleston, SC(Web page, Accessed May 16, 2017 at https://coast.noaa.gov/dataviewer).

Nicholas, A.P., Mitchell, C.A., 2003. Numerical simulation of overbank processes in topographically complex floodplain environments. Hydrol. Processes 17 (4), 727–746.

Nico, G., DiPasquale, A., Corsetti, M., DiNunzio, G., Pitullo, A., Lollino, P., 2015. Use of an advanced SAR monitoring technique to monitor old embankment dams. Engineering Geology for Society and Territory Vol. 6. Springer, Cham, pp. 731–737.

Niedermeier, A., Romaneessen, E., Lehner, S., 2000. Detection of coastlines in SAR images using wavelet methods. IEEE Trans. Geosci. Remote Sens. 38 (5), 2270–2281.

Oberstadler, R., Hönsch, H., Huth, D., 1997. Assessment of the mapping capabilities of ERS-1 SAR data for flood mapping: a case study in Germany. Hydrol. Processes 11 (10), 1415–1425.

Pappenberger, F., Dutra, E., Wetterhall, F., Cloke, H.L., 2012. Deriving global flood hazard maps of fluvial floods through a physical model cascade. Hydrol. Earth Syst. Sci. 16 (11), 4143–4156.

Pradhan, B., Hagemann, U., Tehrany, M.S., Prechtel, N., 2014. An easy to use ArcMap based texture analysis program for extraction of flooded areas from TerraSAR-X satellite image. Comput. Geosci. 63, 34–43.

Pulvirenti, L., Pierdicca, N., Chini, M., Guerriero, L., 2011. An algorithm for operational flood mapping from Synthetic Aperture Radar (SAR) data using fuzzy logic. Nat. Hazard Earth Syst. Sci. 11 (2), 529.

Pulvirenti, L., Pierdicca, N., Squicciarino, G., Boni, G., Chini, M., Benedetto, C., 2016. Polarimetric SAR data for improving flood mapping: an investigation over rice flooded fields. In: Geoscience and Remote Sensing Symposium (IGARSS), 2016 IEEE International. July, IEEE. pp. 7589–7592.

Refice, A., Capolongo, D., Pasquariello, G., D'Addabbo, A., Bovenga, F., Nutricato, R., Lovergine, F.P., Pietranera, L., 2014. SAR and InSAR for flood monitoring: examples with COSMO-SkyMed data. IEEE J. Sel. Top. Appl. Earth Obs. Remote Sens. 7 (7), 2711–2722.

Schellekens, J., Brolsma, R.J., Dahm, R.J., Donchyts, G.V., Winsemius, H.C., 2014. Rapid setup of hydrological and hydraulic models using OpenStreetMap and the SRTM derived digital elevation model. Environ. Modell. Software 61, 98–105.

Schlaffer, S., Matgen, P., Hollaus, M., Wagner, W., 2015. Flood detection from multi-temporal SAR data using harmonic analysis and change detection. Int. J. Appl. Earth Obs. Geoinf. 38, 15–24.

Schmitt, A., Brisco, B., 2013. Wetland monitoring using the curvelet-based change detection method on polarimetric SAR imagery. Water 5 (3), 1036–1051.

Schmitt, A., Wessel, B., Roth, A., 2014. An innovative curvelet-only-based approach for automated change detection in multi-temporal SAR imagery. Remote Sens. 6 (3), 2435–2462.

Schumann, G.J.P., Bates, P.D., Neal, J.C., Andreadis, K.M., 2014. Technology: fight floods on a global scale. Nature 507 (7491) (169-169).

Scussolini, P., Aerts, J.C.J.H., Jongman, B., Bouwer, L.M., Winsemius, H.C., de Moel, H., Ward, P.J., 2016. FLOPROS: an evolving global database of flood protection standards. Nat. Hazards Earth Syst. Sci. 16, 1049–1061.

Tachikawa, T., Kaku, M., Iwasaki, A., Gesch, D.B., Oimoen, M.J., Zhang, Z., Danielson, J.J., Krieger, T., Curtis, B., Haase, J., Abrams, M., 2011. ASTER Global Digital Elevation Model Version 2-summary of Validation Results. NASAhttp://dx.doi.org/10.5194/nhess-16-1049-2016.

Tadono, T., Ishida, H., Oda, F., Naito, S., Minakawa, K., Iwamoto, H., 2014. Precise global DEM generation by ALOS PRISM. ISPRS Ann. Photogramm. Remote Sens. Spat. Inf. Sci. 2 (4), 71.

Takaku, J., Tadono, T., Tsutsui, K., 2014. Generation of high resolution global DSM from ALOS PRISM. Int. Arch. Photogramm. Remote Sens. Spat. Inf. Sci. 40 (4), 243.

Tomás, R., Cano, M., Garcia-Barba, J., Vicente, F., Herrera, G., Lopez-Sanchez, J.M., Mallorquí, J.J., 2013. Monitoring an earthfill dam using differential SAR interferometry: La Pedrera dam, Alicante, Spain. Eng. Geol. 157, 21–32.

Trigg, M.A., Birch, C.E., Neal, J.C., Bates, P.D., Smith, A., Sampson, C.C., Yamazaki, D., Hirabayashi, Y., Pappenberger, F., Dutra, E., Ward, P.J., 2016. The credibility challenge for global fluvial flood risk analysis. Environ. Res. Lett. 11 (9), 094014.

USACE (US Army Corps of Engineers), 2017. National Levee Database. (Web page, Accessed 20 March 2017 at http://nld.usace.army.mil/egis/f?p=471:1).

USGS, 2017. National Water Information System: Web Interface: USGS Water Resources. (Web page, last accessed 24 May 2017 at https://waterdata.usgs.gov).

USGS/NED, 2017. National elevation dataset. The National Map Viewer. Custom Processing of 'USGS NED 1 Arc-second Grdn39w122_13 2013 1×1 degree ArcGrid'. (Accessed March 29, 2017 at https://viewer.nationalmap.gov/basic/).

Wahlstrom, M., Guha-Sapir, D., 2015. The Human Cost of Weather-Related Disasters

1995–2015. UNISDR, Geneva, Switzerland.

Ward, P.J., Jongman, B., Weiland, F.S., Bouwman, A., van Beek, R., Bierkens, M.F., Ligtvoet, W., Winsemius, H.C., 2013. Assessing flood risk at the global scale: model setup, results, and sensitivity. Environ. Res. Lett. 8 (4), 044019.

Westerhoff, R.S., Winsemius, H.C., Huizinga, H.J., Brakenridge, G.R., Bishop, C., 2013. Automated global water mapping based on wide-swath orbital synthetic-aperture radar. Hydrol. Earth Syst. Sci. 17 (2), 651.

White, L., Brisco, B., Dabboor, M., Schmitt, A., Pratt, A., 2015. A collection of SAR methodologies for monitoring wetlands. Remote Sens. 7 (6), 7615–7645.

Winsemius, H.C., Van Beek, L.P.H., Jongman, B., Ward, P.J., Bouwman, A., 2013. A framework for global river flood risk assessments. Hydrol. Earth Syst. Sci. 17 (5), 1871–1892.

Wood, M., Hostache, R., Neal, J., Wagener, T., Giustarini, L., Chini, M., Corato, G., Matgen, P., Bates, P., 2016. Calibration of channel depth and friction parameters in the LISFLOOD-FP hydraulic model using medium-resolution SAR data and identifiability techniques. Hydrol. Earth Syst. Sci. 20 (12), 4983.

Woodcock, C.E., Macomber, S.A., Pax-Lenney, M., Cohen, W.B., 2001. Monitoring large

areas for forest change using Landsat: generalization across space, time and Landsat sensors. Remote Sens. Environ. 78 (1), 194–203.

Wu, H., Adler, R.F., Tian, Y., Huffman, G.J., Li, H., Wang, J., 2014. Real-time global flood estimation using satellite-based precipitation and a coupled land surface and routing model. Water Resour. Res. 50, 2693–2717. http://dx.doi.org/10.1002/2013WR014710.

Yamazaki, D., Kanae, S., Kim, H., Oki, T., 2011. A physically based description of floodplain inundation dynamics in a global river routing model. Water Resour. Res. 47 (4).

Yamazaki, D., O'Loughlin, F., Trigg, M.A., Miller, Z.F., Pavelsky, T.M., Bates, P.D., 2014. Development of the global width database for large rivers. Water Resour. Res. 50, 3467–3480.

Yamazaki, D., Ikeshima, D., Tawatari, R., Yamaguchi, T., O'Loughlin, F., Neal, J.C., Sampson, C.C., Kanae, S., Bates, P.D., 2017. A high-accuracy map of global terrain elevations. Geophys. Res. Lett. 44, 5844–5853. http://dx.doi.org/10.1002/2017GL072874.